Atmos. Chem. Phys., 9, 1209–1225, 2009
www.atmos-chem-phys.net/9/1209/2009/

Atmospheric Chemistry and Physics

Transport mechanisms for synoptic, seasonal and interannual SF_6 variations and "age" of air in troposphere

P. K. Patra[1], M. Takigawa[1], G. S. Dutton[2], K. Uhse[3], K. Ishijima[1], B. R. Lintner[4], K. Miyazaki[1], and J. W. Elkins[2]

[1]Frontier Research Center for Global Change, JAMSTEC, Yokohama 236 001, Japan
[2]NOAA Earth System Research Laboratory, Boulder, CO 80305, USA
[3]Umweltbundesamt – Federal Environment Agency, 63225 Langen, Germany
[4]Department of Atmospheric and Oceanic Sciences and Institute of Geophysics and Planetary Physics, University of California Los Angeles, Los Angeles, CA 90095-1565, USA

Received: 20 May 2008 – Published in Atmos. Chem. Phys. Discuss.: 4 July 2008
Revised: 3 February 2009 – Accepted: 3 February 2009 – Published: 17 February 2009

Abstract. We use an atmospheric general circulation model (AGCM) driven chemistry-transport model (ACTM) to simulate the evolution of sulfur hexafluoride (SF_6) in the troposphere. The model results are compared with continuous measurements at 6 sites over 71° N–90° S. These comparisons demonstrate that the ACTM simulations lie within the measurement uncertainty over the analysis period (1999–2006) and capture salient features of synoptic, seasonal and interannual SF_6 variability. To understand transport timescales of SF_6 within the troposphere, transport times of air parcels from the surface to different regions of the troposphere ("age") are estimated from a simulation of an idealized tracer. The age estimation error and its sensitivity to the selection of reanalysis meteorology for ACTM nudging or the tracer transport by deep cumulus convection as represented in the model are discussed. Monthly-mean, 2-box model exchange times (τ_{ex}) are calculated from both the observed and simulated SF_6 time series at the 6 observing sites and show favorable agreement, suggesting that the ACTM adequately represents large-scale interhemispheric transport. The simulated SF_6 variability is further investigated through decomposition of the mixing ratio time-tendency into advective, convective, and vertical diffusive components. The transport component analysis illustrates the role of each process in SF_6 synoptic variability at the site level and provides insight into the seasonality of τ_{ex}.

1 Introduction

Sulfur hexafluoride (SF_6) represents a powerful tracer of atmospheric transport (Maiss et al., 1996). Emitted at the earth's surface as a byproduct of industrial activity (primarily as a dielectric material in electrical switching equipment), SF_6 has no known production or loss in the troposphere or stratosphere (Ravishankara et al., 1993). Moreover, SF_6 emissions have no significant seasonal cycle. These characteristics render SF_6 ideal for illustrating the effects of different transport processes (e.g. mean meridional transport, convection, vertical diffusion) on the tropospheric distribution of trace species. Like other minor tropospheric constituents, including ^{85}Kr and chlorofluorocarbons (CFCs) (Jacob et al., 1987; Prather et al., 1987), the potential for SF_6 to elucidate tropospheric transport mechanisms has led to its incorporation into model studies, especially as a metric for model intercomparison (e.g. Denning et al., 1999; Law et al., 2008).

While early applications of SF_6 to transport model diagnosis tended to focus on large-scale features such as the interhemispheric gradient, more recent observation-model comparisons of SF_6 (e.g. Peters et al., 2004; Gloor et al., 2007) have demonstrated that current generation transport models are able to resolve finer-scale latitudinal gradients as well as location-specific vertical distributions. The increased capacity of forward transport models to replicate observed SF_6 can be attributed in large part to improvements in the models, including the treatment of diurnally varying planetary boundary layers (PBLs); the refinement of cumulus convective tracer mass transport; and the use of meteorological fields at higher spatial and temporal resolutions to drive advection (see, e.g. Rind et al., 2007 and references therein).

Correspondence to: P. K. Patra
(prabir@jamstec.go.jp)

Published by Copernicus Publications on behalf of the European Geosciences Union.

Table 1. Statistics of model-observation comparison of SF_6; average difference in daily concentrations (Diff.; observation – model), 1-σ standard deviation (SD), and number of observations (N) after taking into account the missing data for two different analysis time periods are given. Note the accuracy in continuous SF_6 measurements is about 0.04 ppt.

Site details				Period: Jan'99 – Dec'06			Period: Jan'03 – Dec'06		
Name	Location			Diff.	SD	N	Diff.	SD	N
	Lat	Lon	Hgt	(ppt)			(ppt)		
BRW	71.3° N	156.6° W	11 m	−0.0059	0.045	2612	−0.036	0.051	1334
NWR	40.0° N	105.6° W	3526 m	−0.015	0.073	1564	−0.025	0.077	898
SCH	47.9° N	7.9° E	1205 m	−0.0085	0.373	1737	+0.0034	0.389	1020
MLO	19.5° N	155.6° W	3397 m	+0.014	0.086	2294	−0.022	0.056	1402
SMO	14.2° S	170.6° W	42 m	+0.017	0.068	2486	+0.00031	0.034	1284
SPO	90.0° S	24.8° W	2810 m	+0.014	0.048	2541	−0.0077	0.043	1335

In the present study, we analyze the characteristics of SF_6 transport as simulated by the Center for Climate System Research/National Institute for Environmental Studies/Frontier Research Center for Global Change (CCSR/NIES/FRCGC) ACTM (hereafter, ACTM for brevity) on daily-to-interannual time scales and local-to-hemispheric space scales. The investigation of ACTM transport variability across multiple temporal and spatial scales is crucial for assessing the model's overall validity for applications such as source/sink inversions of atmospheric CO_2. For example, the inclusion of near-surface land region CO_2 measurement sites in CO_2 inversions may introduce uncertainties into estimated carbon fluxes because of deficiencies or errors in the representation or sampling of such sites in coarse resolution global transport models (Patra et al., 2006, 2008). The present analysis is motivated in part by a recent high-frequency model-observation intercomparison study, TransCom-4 (see Law et al., 2008; Patra et al., 2008) focusing on hourly and daily average CO_2 variations. An important conclusion of TransCom-4 is that the 25 participating models show some skill in simulating the observations, considering uncertainties or errors in CO_2 flux distribution and intensity. However, in that study, detailed analysis of SF_6 as a potential constraint on high-frequency, transport-induced variability was not performed; moreover analysis was further restricted to the period of 2002–2003. Because there are relatively few sites for which high frequency SF_6 data exist, we focus on the continuous observations of SF_6 from 6 sites (WDCGG, 2008; see also Table 1 for a summary of site information), namely Point Barrow (BRW), Schauinsland (SCH), Niwot Ridge (NWR), Mauna Loa (MLO), Samoa (SMO) and South Pole (SPO).

Apart from validating the ACTM's capacity to replicate the SF_6 records from the 6 observing sites, we further examine the roles of different transport processes in explaining variations of SF_6 as simulated by the ACTM. In particular, model simulations are used to analyze the vertical and horizontal features of tropospheric SF_6 transport. To quantify the vertical transport, we make use of an approach commonly applied to the stratosphere (see, e.g. Bischof et al., 1985; Hall and Plumb, 1994) to estimate the age of air in the troposphere. While the age of stratospheric air is usually defined as the time since leaving the tropopause layer, the age of tropospheric air is defined here as time since leaving the earth's surface. The large-scale horizontal transport, readily characterized in terms of an interhemispheric transport time (e.g. Jacob et al., 1987), is computed for both observed and simulated SF_6 data. A more detailed component analysis of ACTM-simulated SF_6 transport elucidates the transport pathways involved in both regional and large-scale atmospheric transport and how these pathways vary on different timescales.

2 Transport model, observations and methodology

2.1 AGCM-based Chemistry Transport Model (ACTM)

The CCSR/NIES/FRCGC AGCM is nudged with reanalysis meteorology using a simple Newtonian relaxation method (Hoke and Anthes, 1976) for driving the chemical tracer transport. The nudging technique forces the AGCM-derived meteorology towards the reanalyzed horizontal winds (U and V components) and temperature (T) with relaxation times of 1 and 2 days, respectively, for every 6-h interval of the reanalysis (except the top and bottom model layers). For the simulations discussed here, we use reanalysis products (U, V, T) from National Center for Environmental Prediction (NCEP)/DOE AMIP-II Reanalysis (Kanamitsu et al., 2002; hereinafter referred to as NCEP2) and European Centre for Medium-Range Weather Forecasts (ERA40, Uppala et al., 2005). To compute the heat and moisture exchange fluxes at the earth's surface, the AGCM is also supplied with interannually varying monthly-mean sea ice and sea-surface temperature (SST) fields from the Met Office Hadley Centre observational datasets (Rayner et al., 2003). This forward transport model has been adapted for simulations of greenhouse gases (CO_2, CH_4, N_2O, CFCs, SF_6 etc.) that have

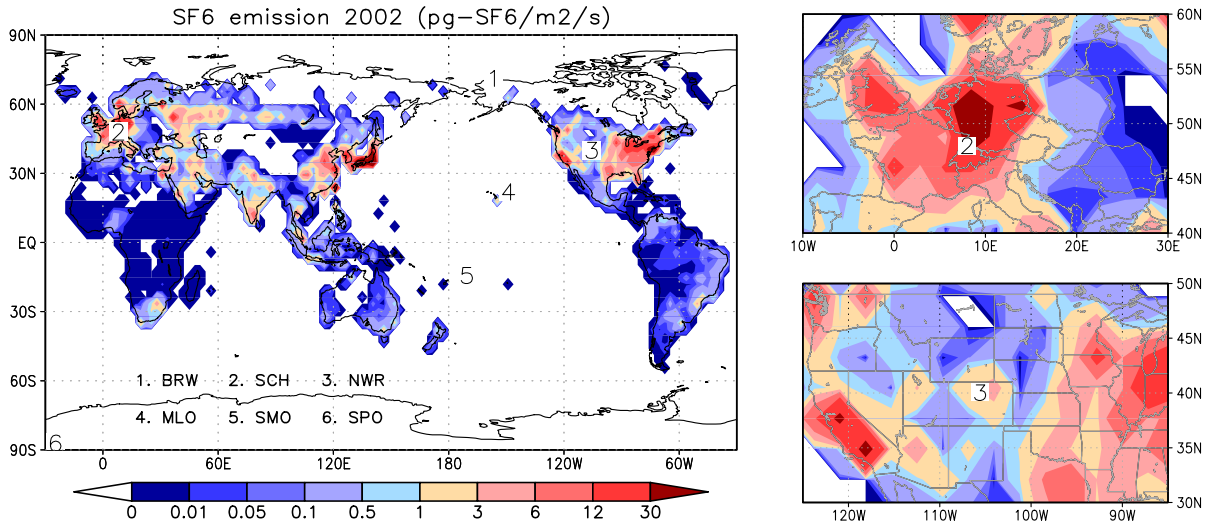

Fig. 1. Distribution of SF_6 emissions (left column; in pg-SF_6 m^{-2} s^{-1}; 1 pg=10^{-12}g) at T42 resolution (~2.8°×2.8° latitude-longitude), with an annual total emission of 8.8×10^9 g-SF_6 yr^{-1} for the year 2002. The measurement site locations are marked as numbers (1–6), with abbreviated names given at bottom-left (see Table 1 for site details). The MLO marker is displaced to the northeast of the site so that the island and emission grid are visible. In the right column are magnified views of the SF_6 emissions around the two continental sites (NWR and SCH).

negligible photochemical production or loss in the troposphere and stratosphere. The ACTM is run in "online" transport mode with both the AGCM meteorology and chemical tracers simulated at the same integration timestep (~20 min). Although computationally expensive, running the ACTM in online mode offers some advantages over less demanding "offline" chemistry-transport models. Specifically, over the period of the analysis, the AGCM generates a detailed and consistent meteorology as represented by the grid- and subgrid-scale processes, surface processes (e.g. PBL height and mixing), above-PBL dynamics (e.g. convection) and interhemispheric gradients.

The basic physical and dynamical features of the ACTM have been described in (Hasumi et al., 2004). Advective transport of moisture and tracers is obtained from a 4th order flux-form advection scheme using a monotonic Piecewise Parabolic Method (PPM) (Colella and Woodward, 1984) and a flux-form semi-Lagrangian scheme (Lin and Rood, 1996). Mass fluxes around the polar caps are calculated with a semi-Lagrangian scheme in polar stereo projection. Subgrid-scale vertical fluxes of heat, moisture, and tracers are approximated using a non-local closure scheme based on Holtslag and Boville (1993) used in conjugation with the level 2 scheme of Mellor and Yamada (1974). The cumulus parameterization scheme is based on Arakawa and Schubert (1974) with some simplifications described in Numaguti et al. (1997). The updraft and downdraft of tracers by cumulus convection are calculated by using the cloud mass flux estimated in the cumulus parameterization scheme.

We use here a relatively coarse resolution, i.e., T42 truncation in the horizontal (approximately 2.8°×2.8°) and 32 vertical sigma-pressure layers up to ~50 km. Although an earlier comparison within TransCom-4 suggests that finer horizontal resolution (e.g., T106 truncation, or ~1.125°×1.125°) does perform better in simulating CO_2 variations at synoptic timescales compared to T42, few systematic differences could be identified between the two resolutions for simulating the CO_2 seasonal cycle or SF_6 interhemispheric gradient (Patra et al., 2008; Law et al., 2008). Overall quality control of the ACTM transport in simulating SF_6 is assessed using recently published data (from Gloor et al., 2007) and is detailed in the supplemental information (http://www.atmos-chem-phys.net/9/1209/2009/acp-9-1209-2009-supplement.pdf) available online (cf., Figs. S1 and S2).

2.2 Fluxes and data for SF_6, and curve fitting

We have simulated SF_6 for overall evaluation of regional and interhemispheric scale atmospheric tracer transport by the ACTM. The SF_6 emissions are taken from the Emission Database for Global Atmospheric Research (EDGAR) (Olivier and Berdowski, 2001), with the yearly emission change scaled to the global SF_6 growth rate estimated from the Earth System Research Laboratory/National Oceanic and Atmospheric Administration, USA (ESRL/NOAA) observations (Geller et al., 1997). The observed concentrations of SF_6 at daily time intervals are taken from the NOAA/ESRL halocarbon in situ network (Butler et al., 2004) and the Air Monitoring Network of Umweltbundesamt, Federal Environmental Agency, Germany (UBA/FEA). The geographic distribution of SF_6 emissions at the ACTM's horizontal

resolution is displayed in Fig. 1 along with the locations of the 6 continuous measurement sites. There is some information loss with the conversion of the raw emission data (at $1^\circ \times 1^\circ$ resolution) to T42, e.g. emissions from the Korean peninsula and Japan are not easily distinguishable, and similarly high emissions from Europe and the United States are smeared out. These errors are denoted hereafter as site representation errors.

Fitted curves and long-term trends for each daily average time series are derived using a Butterworth filter of order 16 (Nakazawa et al., 1997) with a cut-off length of 24 days. The time series are then decomposed into seasonal cycles (data or fitted curves – long-term trends), growth rates (time derivative of the long-term trends) and synoptic variations (data – fitted curves). Statistical assessments of modeled and observed data are determined using original values (without fitting) but excluding missing data periods.

2.3 "Age of air" tracer

The mean "age of air", defined as the time required for an air parcel to transit from the earth's surface to the layers above (Kida, 1983), is calculated as the difference between surface and upper air concentrations normalized by the concentration increase rate at the surface using a Green's function method (Hall and Plumb, 1994). The Green's function is estimated from the simulation of an idealized transport tracer with uniform surface fluxes, linearly increasing trend, and no loss in the atmosphere. Simulation of all tracers was initialized on 1 January 1960 (with the ACTM nudged to ERA40 meteorology; data available up to 2002), and the analysis presented here covers the period of continuous SF_6 observations (ACTM nudged to NCEP2 meteorology; data available from 1979). For the overlapping period of simulations (the 1990s), no significant differences in SF_6 simulations have been found for the two reanalysis products. In a more general sense, systematic differences in simulated synoptic variations of long-lived tracers (e.g., CO_2) using various analysis and reanalysis products in transport models are not evident (see also Patra et al., 2008).

2.4 Two-box model of interhemispheric (IH) exchange time (τ_{ex})

The interhemispheric exchange time (τ_{ex}) has been widely used to diagnose large-scale model transport properties and has been previously estimated from both measured and modeled trace constituents (Jacob et al., 1987; Maiss et al., 1996; Levin and Hesshaimer, 1996; Denning et al., 1999; Geller et al., 1997). τ_{ex} is computed from a simple mass balance equation using the mean mixing ratios and growth rates in the Northern Hemisphere (NH) and Southern Hemisphere (SH) (see, e.g. Prather et al., 1987; Jacob et al., 1987):

$$\frac{dc_n}{dt} = 2\frac{E_n}{\alpha} - \frac{\Delta c_{n-s}}{\tau_{ex}} - \frac{c_n}{\tau_a} \quad (1)$$

$$\frac{dc_s}{dt} = 2\frac{E_s}{\alpha} + \frac{\Delta c_{n-s}}{\tau_{ex}} - \frac{c_s}{\tau_a} \quad (2)$$

Here, c_n and c_s are the average mixing ratios for the NH and SH, respectively; E_n and E_s are hemispheric total tracer emission; α is an emission-to-mixing ratio conversion factor; Δc_{n-s} is the north-south IH difference in tracer mixing ratio; and τ_a is the tracer's atmospheric lifetime. Since SF_6 has no known loss in the atmosphere up to about 50 km and its lifetime as estimated to be about 3200 years (Ravishankara et al., 1993), the last term in both equations can be neglected. Elimation of α from Eqs. (1) and (2) gives an expression for τ_{ex}:

$$\tau_{ex} = \left[\Delta c_{n-s}\left(\frac{E_n}{E_s}+1\right)\right] / \left[\frac{E_n}{E_s}\frac{dc_s}{dt} - \frac{dc_n}{dt}\right] \quad (3)$$

All terms on the right hand side in Eq. (3) are estimated directly from either measured or modeled SF_6 time series. We used the fitted time series and monthly average values for calculation of monthly-mean τ_{ex}.

2.5 Separation of mass transport due to advection, convection and vertical diffusion

Tracer transport in the ACTM comprises numerical solution of the continuity equation that describes the mass conservation for a chemical tracer in the atmosphere:

$$\frac{\partial c}{\partial t} = -\nabla \cdot F + P - L \quad (4)$$

where ∇ is the 3-dimensional divergence operator and F is the tracer mass flux (including both the direct large-scale advective effect and parameterized convection and diffusion terms). P and L are production and loss in the atmosphere, respectively; for SF_6, L is neglected in all model layers, and P=0 at all layers but the surface layer, where the emission occurs. Thus, in the interior of the troposphere, the flux divergence term ($\nabla \cdot F$) associated with various transport processes drives the net time-tendency in c. We decompose the flux divergence term into three components in this study: (1) advection by grid-scale air flow calculated from the flux-form transport scheme (Lin and Rood, 1996); (2) lifting through cumulus convection as parameterized by the Arakawa and Schubert (1974) scheme; and (3) vertical diffusion calculated using the turbulent closure method of Mellor and Yamada (1974). The component tendencies, which are positive (negative) if a model grid gains (loses) mass, are utilized to examine the impact of different transport mechanisms on the temporal evolution of SF_6.

3 Results and discussions

3.1 Model-observation comparison of SF_6 time series

Figure 2 compares observed and simulated SF_6 molar mixing ratios at the 6 continuous observing sites as well as the

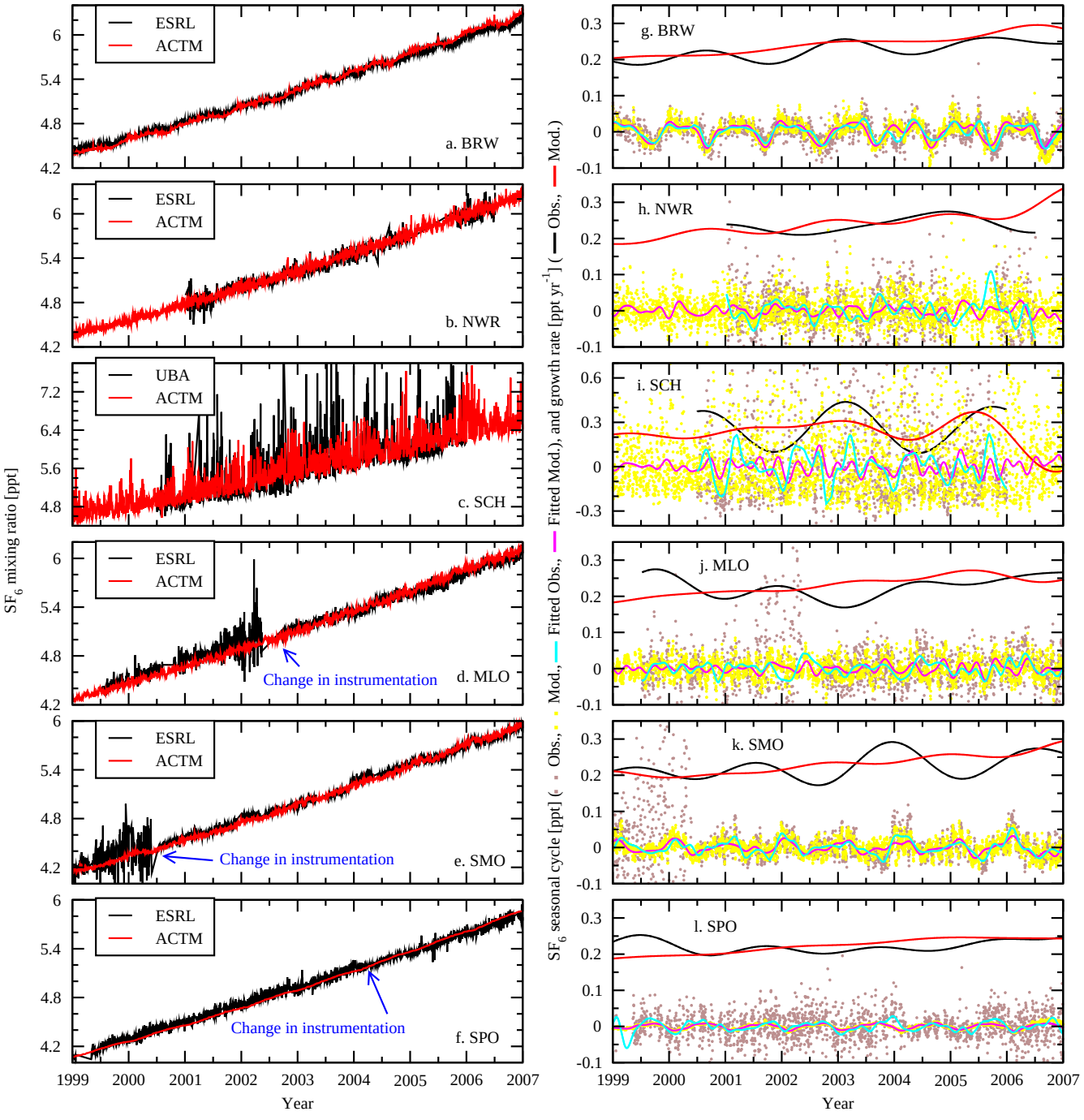

Fig. 2. Comparisons of observed and modeled SF_6 molar mixing ratio (in ppt; ppt=parts per trillion) at 6 sites with continuous observations (**(a–f)**, left column; daily averages, prepared from hourly data, are illustrated here; source: Butler et al. (2004), available online at ftp.cmdl.noaa.gov, path: /hats/sf6/insituGCs/CATS; Uhse et al. (2006), available online at http://gaw.kishou.go.jp/wdcgg). Some changes in measurement instrumentation during the period of comparison are indicated in blue text (see Sect. 3.1 for details). Panels appearing in the right column **(g–l)** show time series decomposed into seasonal cycle and growth rate components at each site (line colours are identified in the right axis title) using the digital filtering technique described in Sect. 2.2.

seasonal cycle and growth rate components of the time series. These results, together with the statistics presented in Table 1, indicate little disagreement between the observed and modeled latitudinal gradients, especially over the Pacific Ocean where the remote background sites BRW, MLO, and SMO are located, and between the continental sites in North America (NWR) and Europe (SCH). In fact, differences between the simulated and observed time series fall within the measurement uncertainty of 0.04 ppt. The amplitude and phasing of the high-frequency variability at all sites are also generally well captured. Some model-observation mismatches do occur, likely arising from spatial representation errors in SF_6 emissions and ACTM transport as well as measurement quality issues.

Over the 1999–2006 period, some changes in observation-model agreement at high-frequencies are evident as instrumentation was altered. For example, marked improvements at SMO and MLO are evident around mid 2000 and mid 2002, respectively, following a change in electron capture detector (ECD). The observed synoptic or finer time scale variability decreased significantly after the detector change, resulting in fluctuations more comparable to the simulations. Also, an ECD change in early 2004 clearly brings the model and observations into closer agreement at SPO, although the agreement deteriorates later in the record. At BRW the modeled concentrations were lower by about 0.05 ppt in 1999 and are higher by about 0.07 ppt in the recent years compared to the observations. Such systematic differences, reflected in the BRW growth rate, may stem from errors in regional emission trends: while the rate of emissions increase in our simulation is globally uniform, the actual trends are likely regionally heterogenous, e.g., larger in rapidly developing countries than in the developed countries. The overall agreement in the latitudinal gradients (Fig. 2, left column) between the simulations and measurements highlights realistic representation of the interhemispheric scale model transport in the ACTM.

The seasonal cycle and its interannual variability (IAV), as derived using the digital filtering method, are fairly well captured by the ACTM simulation at all remote background sites (Fig. 2g, j–l). By contrast, at the continental sites (NWR and SCH), there is no clear seasonality in SF_6 as the IAV is quite large. While the timings of SF_6 increases/decreases generally match between the observed and modeled data, their amplitudes are generally underestimated in the latter, likely as a result of the ACTM's coarse horizontal resolution. Since the SF_6 emissions input to the ACTM lack seasonality, the seasonal variations of simulated SF_6 are driven entirely by atmospheric transport. Poorer agreement at the 2 continental sites compared to the 4 remote sites presumably arises from site representation error within the ACTM's coarse horizontal resolution, i.e. the gridpoint at which the model is sampled may not adequately represent the conditions seen locally at the observing site. The degree to which this type of error contributes may further depend on how the features of local meteorology interact with nearby source emissions (with the latter generally negligible for remote observing sites).

We further illustrate the model-observation agreement of SF_6 synoptic variations at 5 sites (Fig. 3). Here, SPO is excluded because of low signal in the simulation (amplitude variability of $\sim$0.005 ppt or less). As a measure of the phase similarity of modeled and observed SF_6, Pearson's correlation moment (r) values of daily mean SF_6 variability are significant at the 95% confidence interval only at SCH and SMO ($r>0.28$, for $N>600$ data points in Student's 2-tailed test). Normalized standard deviations (NSDs; $=SD_{observation}/SD_{model}$; =1 when modeled and observed variability amplitudes are equal regardless of the phase) are systematically >1 at all sites, indicating smaller variability in the model than in the observations. In the daily-averaged observed time series (thin lines), there are many positive and negative spikes lasting only for a day. Since the ACTM is likely incapable of simulating such sharp spikes because of the smoothed emissions, we also show 5-day (pentadal) running means (thick lines). Visually, the match between simulated and observed synoptic variability improves considerably for the pentadal time series, with both correlations and NSDs improved when 5-day moving window averages (MWAs; 1 average value for each 5-day block in the time series) are considered. Use of 5-day MWAs does not introduce spurious serial autocorrelations into the time series (as is the case for running means) although the length of the time series is reduced by factor of 0.2. Overall, the 5-day MWA correlations at all sites except BRW are found to be statistically significant at the 95% confidence interval ($r>0.41$, for $N\sim125$ data points), while the NSDs are closer to 1 than those estimated from 1-day averages.

From the model-observation comparison, we conclude that the nudged ACTM at T42 horizontal resolution adequately simulates SF_6 interhemispheric mixing ratio gradients, seasonal cycles at remote sites, and synoptic variations at 5-day time scales. Of course, we have also identified some limitations of the coarse resolution global models for simulating the highest-frequency fluctuations of SF_6. In the remainder of this study, we emphasize the simulated transport characteristics that are likely to be significant for SF_6 distributions on regional to global scales and compare some transport diagnostics estimated from observations and model simulations.

3.2 Mean "age of air" in the troposphere and its relation to tracer transport

One of the ways to analyze model transport properties is the age distribution in troposphere, a concept that has been widely applied to tracers in the stratosphere (Bischof et al., 1985; Hall and Plumb, 1994). Here, the mean age has been estimated using the idealized tracer simulation described in Sect. 2.3; latitude-height cross-sections of this timescale are depicted as filled contours in Fig. 4. Throughout much of the troposphere, age values are less than 100 days, which

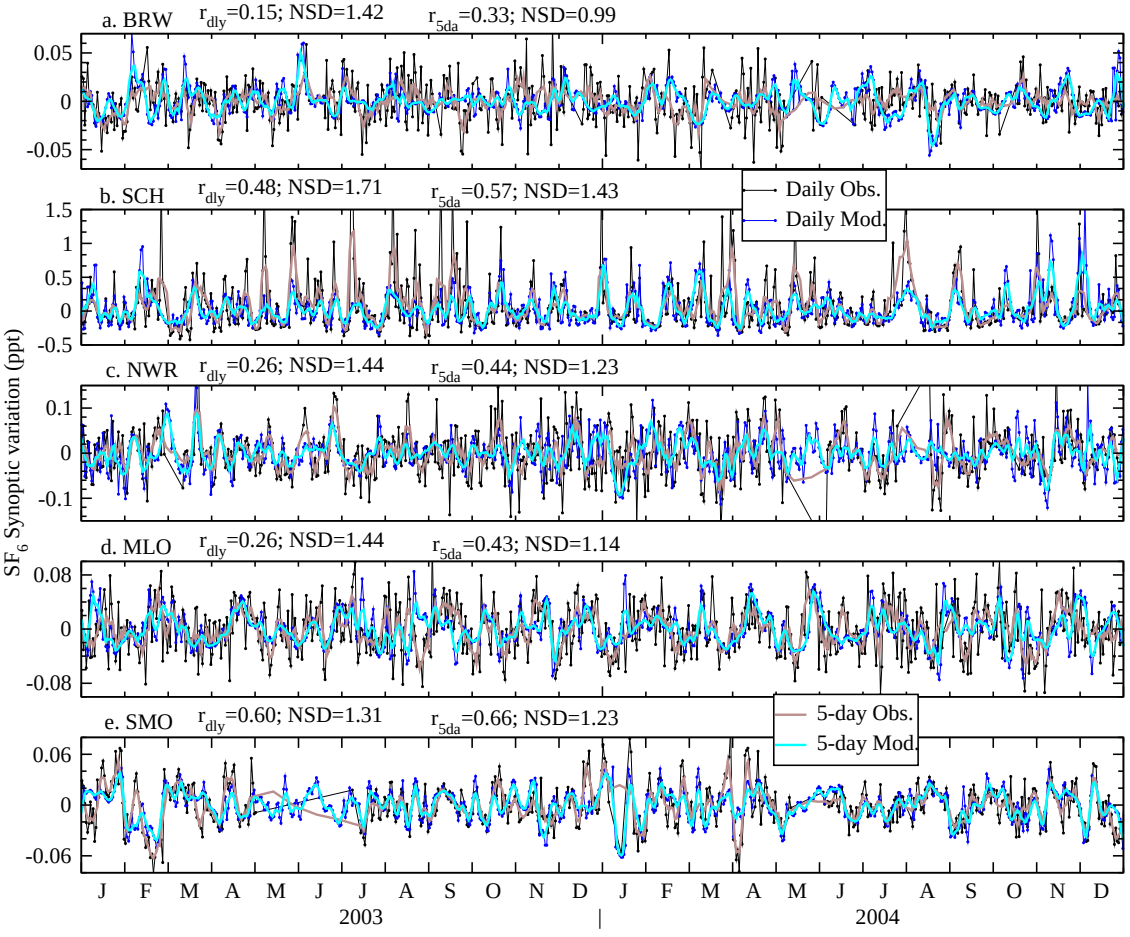

Fig. 3. Synoptic variations in SF_6 at 5 sites (excluding SPO, see Sect. 3.1 for details), derived by subtracting the fitted curve from daily mean values for both models and observations. Daily- and 5-day running means are shown as thin and thick lines, respectively, and the correlation coefficients (r) and normalized standard deviations (NSDs) are given in the panel title for each site. Note the variable y-axis scales in each panel.

are much less than typical values estimated for the stratosphere (i.e., 1–5 years; Bischof et al., 1985), where transport is much slower. The transport model reproduces the upper tropospheric "mixing barrier" around 30° in both hemispheres in most longitude bands and seasons (Erukhimova and Bowman, 2006). The upper tropospheric locations of the steepest meridional age gradients are coincident with the rapid change in zonal winds (black contours) corresponding to the equatorward edges of the subtropical jet steams at approximately 30° latitude in both Hemispheres and between ∼500–150 mb in the vertical. The steep gradient in the age-of-air in the subtropical upper troposphere may be associated with weak breaking of Rossby waves around the level of the θ=350 K potential temperature isotherm (Postel and Hitchman, 1999), as the strong westerlies generally suppress Rossby wave breaking and thus slow mixing. The effect of this mixing barrier has also been discussed in the context of atmospheric CO_2 (Miyazaki et al., 2008).

For the longitude interval spanning the core of the Indian monsoon zone (Fig. 4b), the mixing barrier (defined by large age gradient) lies further north in NH summer because of the extensive cumulus convection near the Himalaya/Tibetan plateau region between 30–40° N. This region bears the signature of younger air at relatively higher altitudes (∼150 mb or higher) in the NH compared to the SH at similar latitudes. Over the Pacific region (Fig. 4c, d), the zone of maximum convection and the upper tropospheric mixing barrier oscillate along with seasonal changes in solar insolation in the absence of heterogeneous orography. Note also that latitudinal gradients in isochrones (contours of constant age) are much steeper in the middle-upper troposphere (∼400 mb and above) of the Indian monsoon region in July (Fig. 4b) compared to January conditions or the mid-Pacific in either January or July (Fig. 4a, c and d).

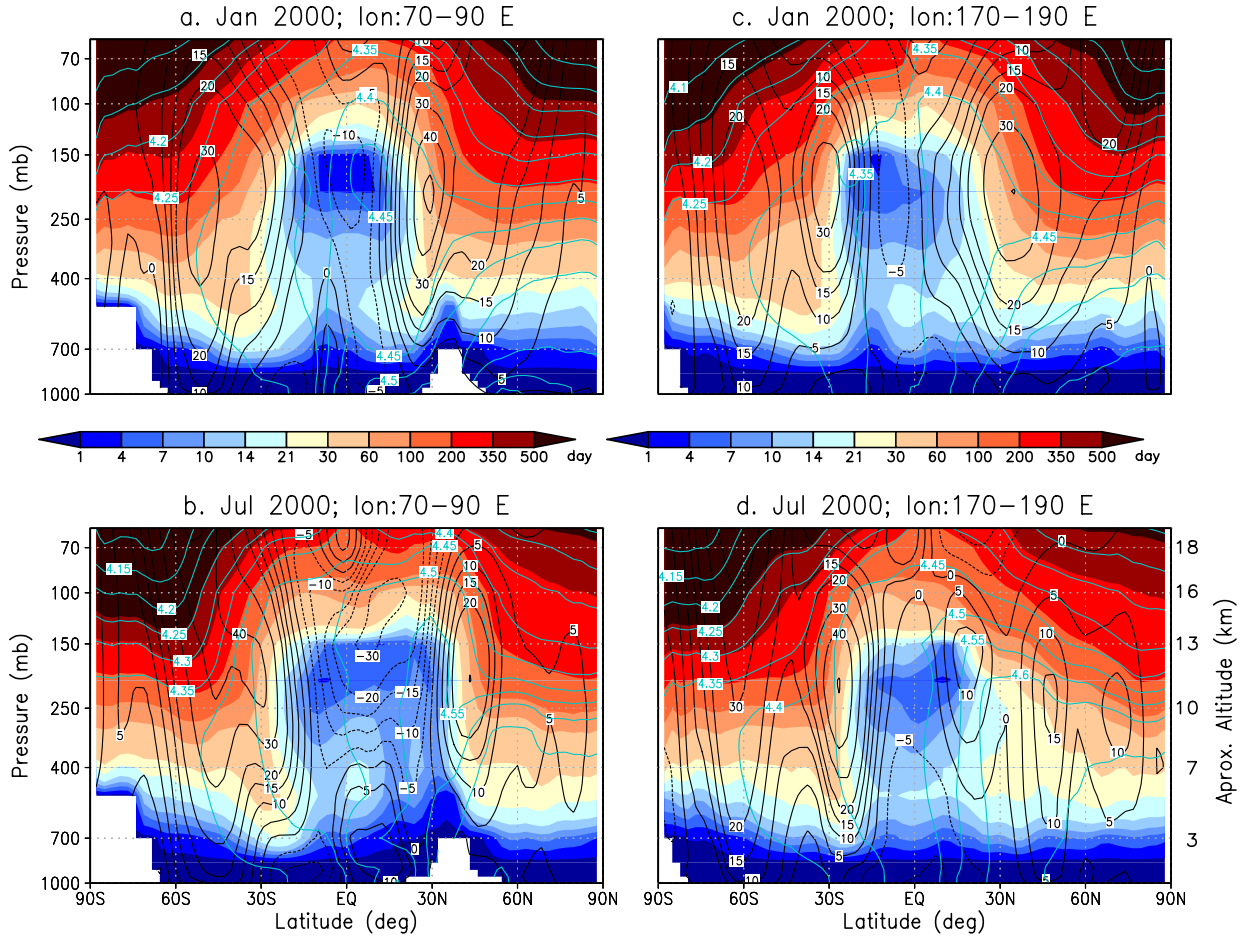

Fig. 4. Latitude-pressure cross-sections of mean age of air (in days) distribution in the troposphere during the NH winter and summer of year 2000 (shaded). Also shown are zonal wind speed (black contour, levels: −20 to 20 at an interval of 5 m s^{-1}, and 30 and 40 m s^{-1}) and SF_6 mixing ratio (light blue contour, levels: 4.1 to 4.7 at an interval of 0.5 ppt) as simulated by the nudged ACTM run. Longitudinal averages are taken along the center of the Indian monsoon zone (left column; panels **a, b**) and the central Pacific (middle column; panels **c, d**). Approximate altitudes (range: ±1 km) corresponding to the pressure levels are labeled on the right y-axis of panel (d). Distributions of potential temperature are shown in Fig. 5. This result is produced using the ACTM nudged to ERA40 meteorology.

Our estimation of the mean age in the tropical upper troposphere, 20–30 days (at the 150 mb model layer; longitude: 87–80° W; latitude: 7–11° N; time: January–February), is within the range of the mean age of air (26±3 days) entering the tropical tropopause as estimated from CO_2 measurements over Central America (latitude: <11° N; height: 14–18 km; time: January–February; Park et al., 2007), although a more extensive data set is necessary to validate the age ranges implied by the modeled age distribution. The smallest vertical age gradients within the troposphere occur mainly where vertical θ gradients (Fig. 4e, f; black contours) are small, i.e. where dynamically or thermodynamically unstable conditions prevail. In the ascending zones of the Hadley circulation, the energy required for air parcels to cross isentropes is mainly supplied through diabatic convective heating/cooling. (The role of individual mechanisms in SF_6 transport is elaborated in Sect. 3.4). The sharp rise in age above the tropopause (θ>400 K and 380 K in the tropics and midlatitude, respectively; note the unequal contour interval with height) is associated with the slower cross-isentropic transport under the strong thermal stratification of the lower stratosphere (i.e., $-\frac{\partial\theta}{\partial P}$ large). Thus, within the tropics, our age distribution calculation supports the conjecture of a vertical mixing barrier in the altitude range of 14 km and tropopause or potential temperature range ∼360–390 K (Folkins et al., 1999), with age increases from a few days below to >100 days above.

We checked the sensitivity of ACTM-simulated age of air by: i) nudging to both NCEP2 and ERA40 meteorology; and ii) disabling tracer transport via parameterized cumulus convection. In the latter (denoted hereafter as NoCumTransp), tracer transport associated with parameterized deep cumulus convection is switched off while the underlying AGCM

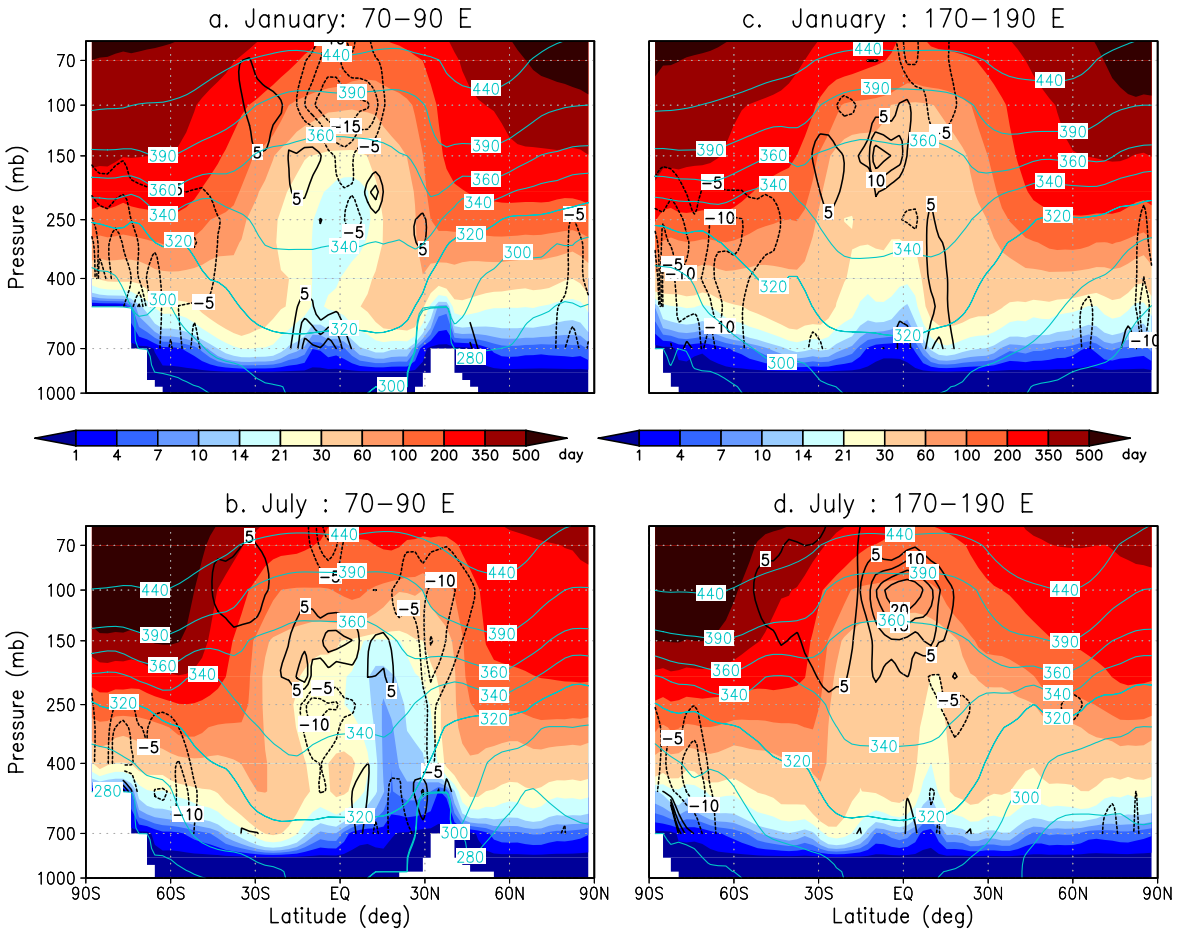

Fig. 5. Latitude-pressure cross-sections of mean age of air as simulated by the ACTM without transport by parameterized cumulus convection for the age tracer (shaded, NoCumTransp case), differences in age between two ACTM simulations by nudging to ERA40 and NCEP2 reanalyzed meteorology (in %; black contour; ERA40-NCEP2), and potential temperature (in K; light blue contour). The seasons (top row: January; bottom row: July) and the locations of longitudinal cross-sections (left column: 70–90° E; right column: 170–190° E) are same as those in Fig. 4a–d.

meteorology is unchanged and nudged to ERA40 meteorology. Figure 5 shows an overall small impact (mostly within 5%; white area) of switching reanalysis meteorology, although there are localized maxima of ∼20% near the latitudes of peak convection. (These localized differences are reduced in the annual mean). On the other hand, rather large differences in age are obtained in the absence of tracer transport by deep cumulus convection. Notably, the age values in the height range of 250–100 mb increase by >60% in the equatorial upper troposphere and up to 10% in the high latitudes in the NoCumTransp case (Fig. 5) relative to the control case (Fig. 4). For these simulations, the effect of cumulus convective tracer transport on monthly mean age is effectively restricted to tropospheric layers and in the tropical lower stratosphere (T-LS; 100–70 mb, 30° S–30° N). The age difference in the T-LS region can be up to 20%, i.e. an absolute difference as large as 30 days. This difference in absolute age is propagated throughout the stratosphere, but it is not significant in a relative sense because of the large age values.

To illustrate the interplay between circulation and age of air, we show the latitude-longitude distributions of age values, vertical/pressure velocity (ω), and horizontal winds at 200 mb in Fig. 6. In the control case, (panels a, b), the regions of youngest air (darkest blue shading) at this height are always colocated with the strongest grid-scale upward motion (red contours), particularly when the age signatures indicate tropospheric air. In the NoCumTransp case, there is a weak association between small age values and upper level horizontal wind divergence, with non-neglible gradients only near the Asian monsoon/western Pacific warm pool region (where convection is strongest) (Fig. 6c, d). These results underscore the importance of parameterized convective tracer transport for species with atmospheric residence times comparable to the age of air in the troposphere: chemical constituent with atmospheric residence times less than 30

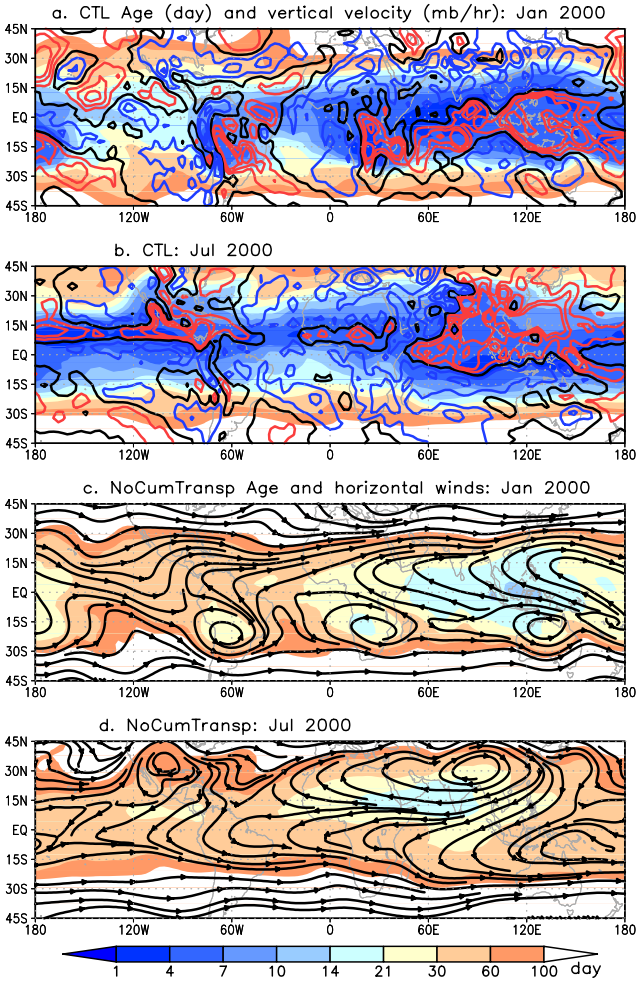

Fig. 6. Longitude-latitude distributions of ACTM simulated vertical velocity contours (at −1.0, −1.0, −0.5 (red line; upward motion), 0 (black line), 0.5, 1.0, 1.5 (blue line; downward motion) mb hr^{-1}) overlaid on the age (shaded) at 200 mb are shown in top two panels (referred as Control simulation, CTL). Bottom two panels (c, d) are showing the age distribution for NoCumTransp case and horizontal wind streamlines being overlaid. Note that the horizontal and vertical velocities are identical for CTL and NoCumTransp simulations. Age values >100 days, denoting stratospheric air, are whitened.

days (i.e., the approximate age of air at 200 mb for NoCumTransp case) would be unable to reach the upper troposphere in the absence of transport via parameterized cumulus convection. Even in the control, the transport efficiency of chemical species with short residence times (days to weeks) from the earth's surface to various parts of the upper troposphere/lower stratosphere (UT/LS) will strongly depend on the location of emissions and season.

In ACTM framework, cumulus convective transport in the tropics is far more effective in vertical mass delivery from earth's surface to the upper troposphere at short timescales than is the large-scale advective transport shown by the winds fields. This is presumably because of the lack of a connection between the mixing in lowermost troposphere by vertical diffusion and relatively strong winds divergence in the upper troposphere. Note also that the large-scale monsoon anticyclones, centered near 130° E, 15° S in January and 90° E, 20° N in July, produce sharp age gradients by restricting air mass transport across the southern and northern edges, respectively. At the same time the aniticyclones transport low age air across the equator.

For the long-lived trace constituents like SF_6, the link between increasing age of air in the (lower) stratosphere and decreasing mixing ratio is clearly seen (Fig. 4), as the isochrones and SF_6 isopleths are parallel to each other for the altitude range where age is greater than 100 days. In the NH troposphere for latitudes poleward of 40° N, age is increased and SF_6 mixing ratios decrease with altitude, particularly during the NH winter when convective transport is weaker. The SF_6 isopleths tend to become vertical on encountering the NH mixing barrier. In the tropics SF_6 is always well mixed vertically, and a strong latitudinal gradient is established around the subtropics. The meridional mixing ratio gradient weakens in the SH mid- and high-latitudes. These characteristics of SF_6 make it a powerful tracer for studying interhemispheric exchange in the troposphere as well as large-scale dynamical processes in the lower stratosphere.

3.3 Interhemispheric exchange time

Monthly-mean τ_{ex} estimated from both ACTM-simulated and observed SF_6 data appear in Fig. 7. For comparative purposes, hemispheric average mixing ratios were calculated from a few different combinations of the 4 NH and 2 SH sites. For case 1 (Fig. 7a, light blue), all sites in each hemisphere were used in the averaging, while in case 2 (black) only the remote sites (BRW, MLO, SMO, and SPO) were used. The τ_{ex} values are lower in case 2, which reflects exclusion of the non-background, high-concentration sites at NWR and SCH. Somewhat smaller values of τ_{ex} are evident for case 2 (black), in which only the SF_6 mixing ratios at the remote sites were used in averaging. For case 3 (dark blue), which used MLO and SMO concentrations as proxies for the NH and SH hemispheric averages, the lowest mean exchange times were obtained, resulting from the relatively small difference in mixing ratio between these close proximity sites, although the variability is clearly the largest. An additional case (4, black line; Fig. 7b), calculated from the ACTM simulation only using the average surface mixing ratio for all NH and SH gridpoints, produces similar τ_{ex} estimates to case 2, suggesting that SF_6 hemispheric averages consisting of BRW and MLO in the NH and SMO and SPO in SH are representative of the whole hemispheric averages.

Values of annual mean τ_{ex}, computed for the various cases, are summarized in Table 2 along with several estimates from prior studies. Both the observed and simulated results obtained in cases 1 and 2 compare well with the estimates of

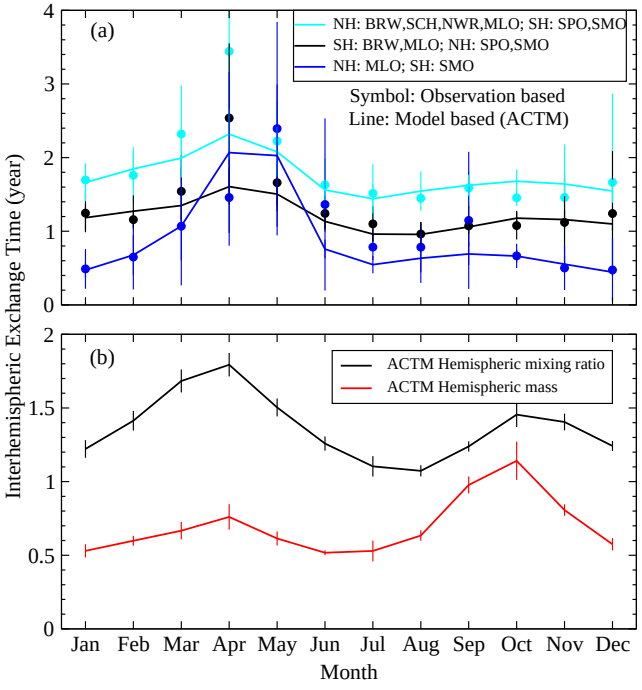

Fig. 7. Climatological average (period: 2001-2005) monthly-mean inter-hemispheric exchange time as estimated from SF_6 model simulation (line) and observations (symbol) at 6 sites and their three combinations to calculate hemispheric mean concentrations (top; panel **(a)**; light blue: Case 1, black: Case 2, dark blue: Case 3). Bottom panel **(b)**; black line: Case 4, Red line: Case 5 shows exchange times estimated using model based the hemispheric mean mixing ratio at the surface and total mass in the troposphere (surface to 100 mb). Note the difference between two y-axis scales.

Levin and Hesshaimer (1996) and Geller et al. (1997), despite the interannual variability in τ_{ex}. We point out that some differences between different studies may be tied to the selection of station sets for estimating the hemispheric average mixing ratios. The ACTM-derived τ_{ex} are also in the range of earlier SF_6 model-based estimates of 0.76–1.97 years obtained from multiple transport models (Denning et al., 1999). However, the more recent TransCom-4 intercomparison (Law et al., 2008) demonstrates much tighter agreement in SF_6 IH gradients. Specifically, 17 out of 20 global models examined produced IH gradients in the range of 0.21–0.29 ppt (0.24 ppt for the ACTM at T42) compared to an observed value of 0.23 ppt (for 2002), implying less spread among the TransCom-4 τ_{ex} estimates. The closer agreement among models in the more recent intercomparison likely reflects improvements in forward transport modeling; moreover, all TransCom-4 models used analyzed meteorology to drive model transport, while in the Denning et al. intercomparison, modeling groups chose the meteorology divers independently (e.g. reanalysis or GCM winds). For case 4 as well as an analogous calculation using the total 3D mass distribution within the troposphere (case 5), annual-mean τ_{ex} values of 1.37 (case 4) and 0.7 (case 5) years are obtained. The case 5 estimate is within the range of 0.55–1.26 years noted by Denning et al. (1999) and more closely agrees with recent model estimates of ∼0.7–1.20 years (ref. Table 2).

The monthly-mean τ_{ex} manifest pronounced seasonal cycles in all cases considered here. In particular, the seasonality is dominated by a semi-annual periodicity for cases 4 and 5 (Fig. 7b). The primary and secondary maxima, corresponding to relatively slow IH exchange rates, are found during April and October, respectively, and minima occur during January and July (case 4; note the reversal of the primary and secondary maxima in case 5.) This seasonality is similar to that described in Lintner et al. (2004) but is distinct from the seasonality shown in Levin and Hesshaimer (1996). Broadly, such seasonality can be understood in terms of the seasonal variations in the Hadley circulation and the meridional displacement of Intertropical Convergence Zone (ITCZ), with the solisticial seasons of strong and equatorially asymmetric Hadley cells producing strong cross-equatorial flow and more rapid exchange of tracer mass (Lintner et al., 2004). In fact, idealized model studies suggest that seasonal oscillation of the Hadley circulation may be responsible for a significant portion of IH mixing (Bowman and Cohen, 1997). A more complete picture of τ_{ex} seasonality in the ACTM is developed below.

The model-observation mismatches in April are mainly caused by the variability in the Samoa (SMO) site data. This site is situated between the western Pacific ITCZ and South-Pacific Convergence Zone (SPCZ) and is significantly influenced on interannual timescales by El-Nino Southern Oscillation (ENSO)-induced transport variability. For instance, we find the smallest dC_s/dt values at SMO during 2001 and 2002 April, which is coincident with a period of sharp increase in Multivariate ENSO Index (MEI). Low mixing ratios at SMO during El Niño events have been attributed to locally-enhanced southeasterly flow at the surface associated with a northward shift of the SPCZ (Hartley and Black, 1995). Omitting anomalous SMO outliers in the averaging yields observational (simulated) τ_{ex} values of 2.7 (2.3), 2.1 (1.6) and 1.8 (1.5) years for Case 1, 2 and 3, respectively.

3.4 Analysis of SF_6 transport pathways and seasonality in τ_{ex}

Tropospheric tracer transport in the ACTM consists of advection, convection, and vertical diffusion as described in Sect. 2.5. Figure 8 shows latitude-pressure distributions of Eulerian mean SF_6 mass transfer rates of each of these components. Generally, the advection term dominates in most parts of the troposphere, with the intensity maximized ($\geq$1 pptm/mon) over 30° S–60° N, where the meridional gradient in SF_6 is the largest (black contours in Fig. 8a–d). In a globally-averaged sense, cumulus convective transport is the next largest term, although it is principally localized to

Table 2. Comparison of τ_{ex} (in year) between the model- and observation-based estimates found here and previously published estimates using SF_6 (LH96: Levin and Hesshaimer; LG97: Geller et al.; SD99: Denning et al., 1999; BL04: Lintner et al.; DR07: Rind et al. [horizontal resolution: 3.2×2.5°]; AA08: Aghedo et al. [ERA-40 case]). For the results obtained here, error values corresponding to one standard deviation (1σ) are given, with σ calculated from annual mean values for the period 2001–2005, indicating the amplitude of interannual variability in τ_{ex}. The results obtained from multi-model transport are given as "range".

τ_{ex} Estimation Method	ACTM Based Mean±1σ	Observ. Based Mean±1σ	LH96 Mean	LG97 Mean	SD99 Range	BL04 Range	DR07 Range	AA08 Mean
Site based estimates								
Case 1	1.75±0.03	1.86±0.16	1.50	1.30				
Case 2	1.21±0.01	1.33±0.18						
Case 3	1.07±0.40	0.99±0.31						
Whole Hemisphere Based Estimates								
Case 4	1.37±0.04				0.76–1.97			
Case 5	0.70±0.01				0.55–1.26	0.80–1.2	0.78–1.02	0.70

tropical and sub-tropical latitudes where it efficiently transfers mass from surface levels to the upper troposphere (see also Donner et al., 2007). Vertical diffusion plays a major role only near source emission regions (land areas between 20–60° N latitude; see Fig. 1) where low-level loadings of SF_6 are maximized. Figure 8e–h and f–i indicate that the tracer transport associated with parameterized convection is limited to the top of the Hadley cells, which has been suggested as a cause for the vertical mixing barrier in the tropical upper troposphere (see also Folkins et al., 1999). The average upper height limit for convective detrainment is located around 14 km, coinciding with the largest age gradient (>25 day/km) below the tropical tropopause (altitude range of 14–16 km).

To summarize the typical transport pathway connecting the source regions to remote portions of the troposphere, SF_6 emissions are initially mixed through vertical diffusion near the source regions (shown in red in Fig. 8i–l). Except for the emission layer (model level #1), the model levels up to ∼500 mb between roughly 30–60° N gain SF_6 through vertical diffusion. From here, SF_6 is lofted deeper into the upper troposphere by convective transport from the lower troposphere (Fig. 8e–h). In regions of strong convection near the equator, the spacing between isentropes is reduced, facilitating efficient and strong vertical mass transport in this part of the troposphere. Generally, increases to upper tropospheric SF_6 mixing ratios via convective transport are restricted to the north side of the upward branch of the Hadley circulation; to the south, upper tropospheric SF_6 values are reduced by convective uplift of low tropospheric air masses since the near-surface SH air is relatively deficient in SF_6. Negative values of the Eulerian mean pressure velocity (ω), contoured in the right column of Fig. 8, correspond to large-scale ascent, with the strongest upward motion of the Hadley circulation located around 15° S (15° N) during boreal winter (summer). Note that the Eulerian mean circulation does not accurately represent the Lagrangian (tracer) circulation in the extratropics (see Bowman and Carrie, 2002 for details). Upon its delivery to the middle and upper troposphere, SF_6 is advected longitudinally by strong zonal winds. Miyazaki et al. (2008) discuss detailed mechanisms of tropospheric CO_2 transport, with the results presented here supporting their conclusions. Relative to CO_2, the SF_6-based analysis is easier to visualize because of simpler emission statistics (i.e. well-defined source emission regions with no seasonality), and the simulated data can be readily validated against observations through simple transport diagnostics like τ_{ex}.

The Hadley circulation and its associated meridional winds advect SF_6 into the Tropics. The seasonality of τ_{ex} mirrors seasonalities seen in the convective and advective transport components of SF_6 near the equator. Figure 8e and g indicates that the maximum SF_6 transport to the upper troposphere associated with parameterized convection occurs near the equator, while Fig. 8a, c shows upper tropospheric meridional spreading of SF_6 by advection across mixing ratio isopleths. This situation accounts for the faster tracer mass transport across the equator during January and July. On the other hand, during April and October, the regions of strong advective transport in the tropical upper troposphere do not cross the SF_6 mixing ratio isopleths. The apparent isolation of SF_6 transport on either side of the equator during the equinoctal seasons is consistent with the larger 2-box exchange times estimated from measured and simulated SF_6. Results of a recent study by Aghedo et al. (2008) suggest that the seasonal asymmetry in τ_{ex} should be opposite for tracer emissions localized to the SH, with the primary (secondary) maximum in October (April), although the reason for such sensitivity is unclear.

The location of mixing barriers, particularly over the NH, determine the intensity of meridional tracer advection. When

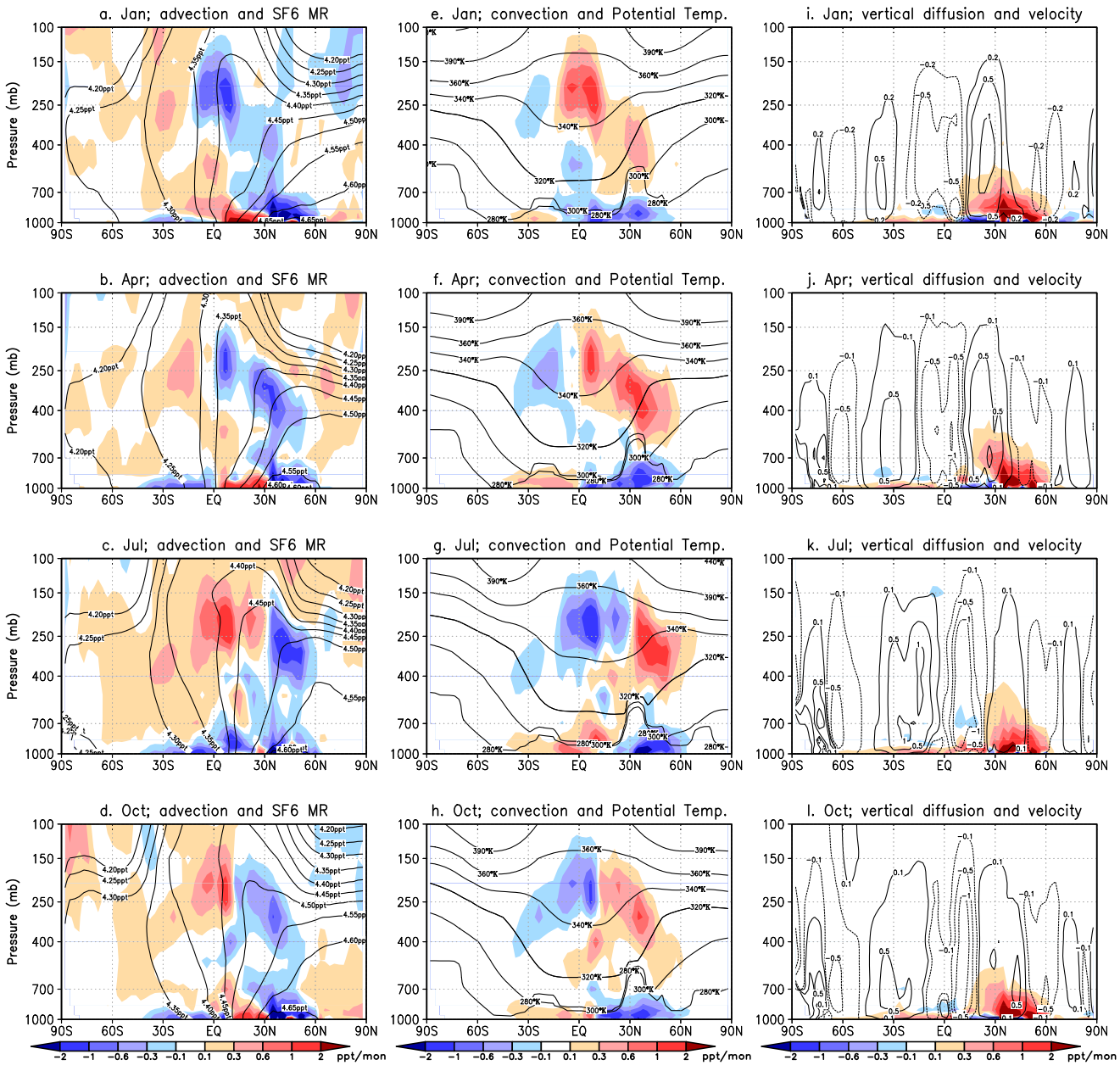

Fig. 8. Monthly and zonal average distributions of component SF_6 mass mixing ratio (MR) tendencies (in pptm month^{-1}) as modeled in the ACTM for the year 2000; panels **(a–d)** (left column): transport by grid-scale advection, **(e–h)** (middle column): convective transport, i-l (right column): vertical transport by diffusion (shaded). The black contours shown denote SF_6 mixing ratio (a–d; unit ppt); potential temperature (e–h; unit K); and vertical velocity (**(i–l)** unit: mb hr^{-1}). These contours are provided for interpreting relationships between the meteorological conditions and transport components as discussed in Sect. 3.4.

the NH mixing barrier is located at about 15° N during January (at the downwelling branch of the Hadley circulation), the cross-equatorial mass transfer in the upper troposphere is minimized and intensified in the lower troposphere (below 700 mb). In fact, the strong subsidence leads to reduction (enhancement) of high SF_6 in the upper (lower) troposphere. The situation is opposite during July, when the NH mixing barrier is located over 40° N (the region of strongest SF_6 emission). The upwelling branch of the Hadley circulation (between 0–25° N latitude) transfers SF_6 rich air to the upper troposphere from lower troposphere, which is then transported to the SH by the meridional branch of the Hadley cell in the height range of 150–250 mb.

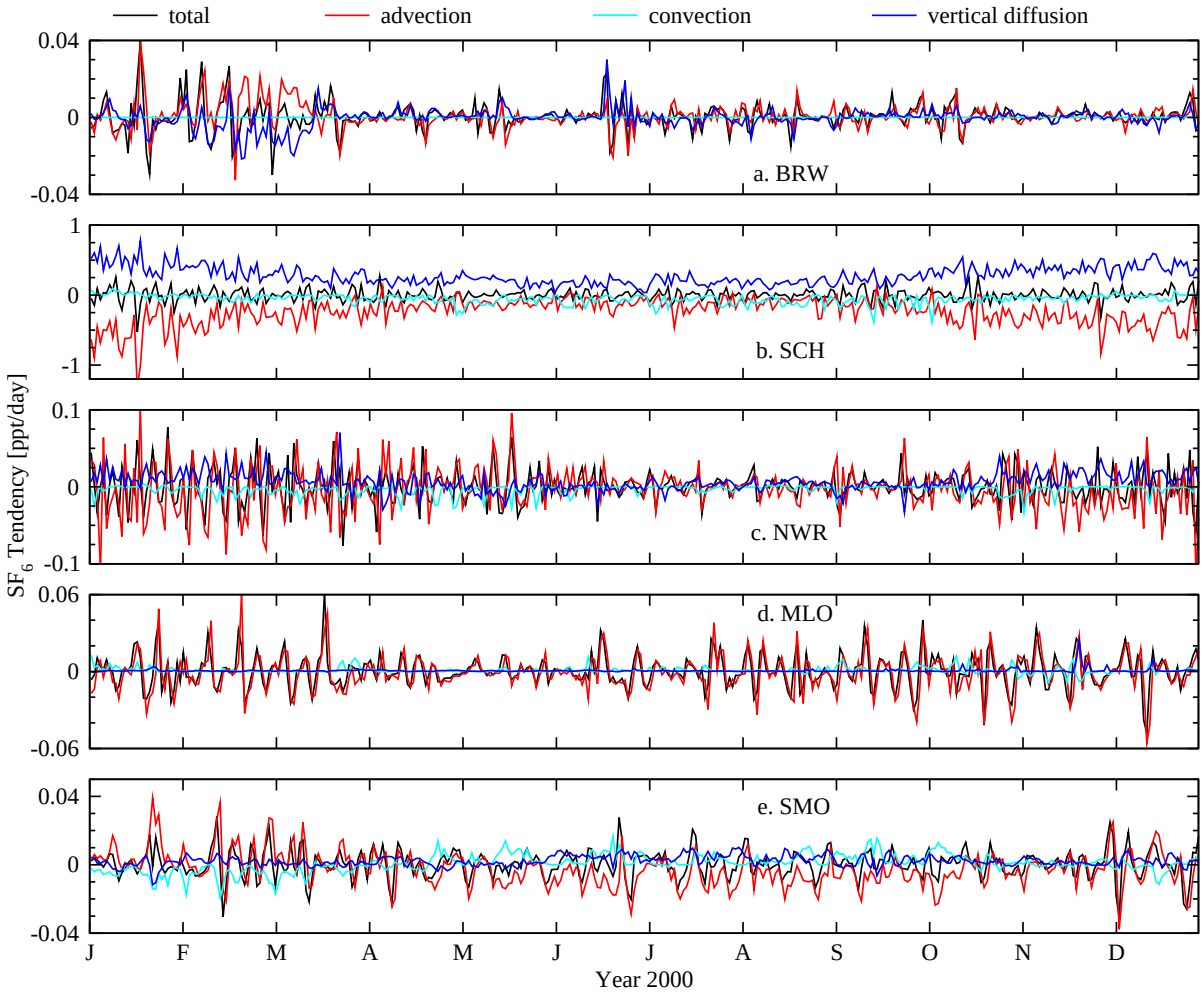

Fig. 9. Total tendencies of modeled SF_6 mixing ratio and the three transport components at 5 sites are shown (in ppt/day). Averages are taken over 5 model grids (nearest sampling grid plus 4 neighboring grids at the same sigma-pressure level) in order to reduce high frequency variations.

3.5 Contributions of transport pathways to SF_6 synoptic variations at surface sites

The transport components for the 5 continuous monitoring sites excluding SPO are presented in Fig. 9. It is clear that, depending on site location with respect to major emission regions and atmospheric transport regimes, the dominant mechanism(s) for SF_6 variability differs. The tendency components also exhibit distinct seasonality at some sites. At BRW, transport by advection (red) dominates in January when the winds are predominantly northerly. By contrast, during February–March, under the influence of stronger southerly flow, both advection and vertical diffusion (blue) are comparable and generally of opposite phase, thereby attenuating the total synoptic-scale variability. At SCH, the antiphasing of synoptic SF_6 transport via advection and vertical diffusion is clearer. Advective and vertical diffusive tendencies are largest during the boreal winter, when PBL ventilation is weak, and smallest during the boreal summer, when PBL ventilation is strong: at SCH (located at 1205 m altitude), the maximum PBL height simulated by the ACTM is typically 400 m during winter, but it is as high as 1500 m during the summer. It is important to note that the simulated SF_6 at SCH was sampled at model level 3, even though the site is actually located on a mountain top, i.e. locally the earth's surface, which strictly corresponds to model level 1 in the sigma-pressure coordinate. At the other continental site, NWR, the synoptic variability of advective transport is much larger than the vertical diffusive component; however, the magnitude of variability at NWR is several times smaller than that at SCH because of differences in SF_6 emission in their proximity (cf. Fig. 1; right column). At the remote MLO site, the synoptic variation in SF_6 is almost entirely driven by advection. Only at the remote marine site SMO is the convective transport (in cyan) of comparable magnitude

to the advective transport at synoptic timescales. Interestingly, these two components are out of phase, with the tendencies changing sign seasonally, e.g. advection (convection) shows positive (negative) tendencies during January–February and negative (positive) tendencies during March–September. These features can be understood from changes in SF_6 vertical structure and the Hadley circulation as seen in Fig. 8.

However, it is worth noting that an accurately simulated SF_6 distribution alone does not imply that the relative influences of advection and convection are accurately modeled in ACTM. Checking some fundamental model properties against observations provides some confidence in the fields used to drive tracer transport. For example, comparison of the simulated outgoing longwave radiation (OLR) aginst the NOAA non-interpolated OLR (source: www.cdc.noaa.gov) on daily and monthly timescales suggests reasonable simulation of the intensity and location of tropical convection zones. Additionally, a multi-tracer (CO_2, CO, O_3) analysis using nudged and free (without U, V, T nudging) meteorology showed closer agreements between the simulated and observed daily-averaged tracer and OLR variations for the nudged ACTM results compared to the free running ACTM (Patra et al., 2007). Further relevant observables to identify and validate the relative partitioning of advection and convection in models, e.g., vertical profiles of trace species with varied atmospheric residence time and well constrained surface fluxes, are clearly desirable.

4 Conclusions

The CCSR/NIES/FRCGC AGCM-driven online transport model (ACTM) has been applied to simulate atmospheric SF_6. These simulations prove comparable to the observed behavior at six continuous measurement sites, with mixing ratios increasing by about 1.6 and 1.8 ppt and at SPO (90° N) and BRW (71° S), respectively, between 1999 and 2006. Both the modeled and measured time series are decomposed into synoptic variations, seasonal cycles, and growth rates, with the synoptic and seasonal variations of simulated and observed SF_6 data correlating significantly at most sites during the analysis period. The ACTM is thus a useful tool to study daily- to yearly- transport mechanisms in the troposphere.

An illustrative transport metric for the ACTM discussed here is the tropospheric "age of air", with age values agreeing with available observation-based estimates of order 20–30 days in the tropical upper troposphere. However, more observations are required for spatially extensive validation of tropospheric age estimates. We have shown small error could arise in age estimation of tropospheric air due to nudging the ACTM with NCEP2 or ERA40 meteorology. On the contrary, removing the effect of cumulus convection on tracer transport in the ACTM results in significant lengthening of age estimates; thus, the accuracy of cumulus convection parameteriztions and their impact on tracers have large implications for the distributions of chemical sepcies in the upper troposphere/lower stratosphere. Additionally, the 2-box interhemispheric exchange times (τ_{ex}), estimated using observed ($\sim$1.3 year) and modeled ($\sim$1.2 year) surface SF_6 mixing ratios, agree well with prior estimates based on earlier simulations/observations. While the exchange time is found to be dependent on the details of the hemispheric mean SF_6 mixing ratio estimates, the combination of BRW and MLO in the NH and SMO and SPO in the SH reasonably represents their respective hemispheric mean surface mixing ratio for SF_6. The seasonality in τ_{ex} is shown to arise primarily from the seasonal migration of the zonal mean meridional advective transport across the equator: stronger isolation of the NH (high SF_6 air) and the SH (low SF_6 air) occurs during boreal spring (April) and autumn (October), resulting in the slowest net cross-equatorial exchange of tracer mass.

From the tracer transport component tendency perspective within the ACTM, vertical diffusion accounts for much of the delivery of SF_6 from its surface emission regions into the lower troposphere, after which tracer mass transport to the sub-tropical and tropical upper troposphere is accomplished largely by the effect of parameterized cumulus convection. The maximum mass exchange between the hemispheres occurs in the upper troposphere region via advection, which gives produces smaller 2-box exchange times if the total SF_6 hemispheric mass is considered instead surface-only values. The transport component analysis is further illustrates the relative roles of the three different transport processes at individual sites, with sizable differences in the relative transport partitioning evident for different locations.

Overall, our study demonstrates that the ACTM adequately simulates the transport characteristics of potential relevance to inverse modeling or data assimilation of atmospheric trace species such as CO_2, CH_4, and N_2O. In a follow-up study, we use the ACTM to perform a CO_2 inversion analysis of weekly measurements to estimate high-frequency regional CO_2 fluxes. Given the ACTM's capacity to replicate observed SF_6 without notable bias or error at regional and hemispheric scales, we have some confidence that inverse-estimated regional CO_2 fluxes will reflect proper treatment of atmospheric transport.

Acknowledgements. This work is partly supported by the Grants-in-Aid for Creative Scientific Research (2005/17GS0203) of the Ministry of Education, Science, Sports and Culture, Japan. We appreciate the support of Takakiyo Nakazawa and Hajime Akimoto for this research, and we thank Bradley Hall for creating and maintaining the NOAA/ESRL 2006 SF_6 scale. BRL acknowledges the support of National Science Foundation ATM-0645200 (J. D. Neelin, PI). Comments and suggestions from Jessica Neu, an anonymous reviewer, and Peter Haynes were helpful for revising the article.

Edited by: P. Haynes

References

Aghedo, A., Rast, S., and Schultz, M. G.: Sensitivity of tracer transport to model resolution, forcing data and tracer lifetime in the general circulation model ECHAM5, Atmos. Chem. Phys. Discuss., 8, 137–160, 2008, http://www.atmos-chem-phys-discuss.net/8/137/2008/.

Arakawa, A. and Schubert, W. H.: Interactions of cumulus cloud ensemble with the large-scale environment, Part I, J. Atmos. Sci., 31, 671–701, 1974.

Bischof, W., Borchers, R., Fabian, P., and Krüger, B. C.: Increased concentration and vertical distribution of carbon dioxide in the stratosphere, Nature, 316, 708–710, 1985.

Bowman, K. P. and Cohen, P.: Interhemispheric exchange by seasonal modulation of the Hadley circulation, J. Atmos. Sci., 54, 2045–2059, 1997.

Bowman, K. P. and Carrie, G. R.: The mean-meridional transport circulation of the troposphere in an idealized GCM, J. Atmos. Sci., 59, 1502–1514, 2002.

Butler, J. H., Daube, B. C., Dutton, G. S., Elkins, J. W., Hall, B. D., Hurst, D. F., King, D. B., Kline, E. S., Lafleur, B. G., Lind, J., Lovitz, S., Mondeel, D., Montzka, S. A., Moore, F. L., Nance, J. D., New, J. L., Romashkin, P. A., Scheffer, A., and Snible, W. J.: Halocarbons and Other Atmospheric Trace Species, Chapter 5, in: CMDL Summary Report No. 27, 2002–2003, NOAA/US Department of Commerce, edited by: Thompson, T. M., Boulder, USA, 115–135, 2004.

Colella, P. and Woodward, P. R.: The Piecewise Parabolic Method (PPM) for Gas-Dynamic Simulations, J. Comput. Phys., 54, 174–201, 1984.

Denning, A. S., Holzer, M., Gurney, K. R., Heimann, M., Law, R. M., Rayner, P. J., Fung, I. Y., Fan, S., Taguchi, S., Friedlingstein, P., Balkanski, Y., Maiss, M., and Levin, I.: Three-dimensional transport and concentration of SF_6: A model intercomparison study (Transcom 2), Tellus, 51B, 266–297, 1999.

Donner, L. J., Horowitz, L. W., Fiore, A. M., Seman, C. J., Blake, D. R., and Blake, N. J.: Transport of radon-222 and methyl iodide by deep convection in the GFDL Global Atmospheric Model AM2, J. Geophys. Res., 112, D17303, doi:10.1029/2006JD007548, 2007.

Erukhimova, T. and Bowman, K. P.: Role of convection in global-scale transport in the troposphere, J. Geophys. Res., 111, D03105, doi:10.1029/JD006006, 2006.

Folkins, I., Lowewenstein, M., Podolske, J., Oltmans, S., and Proffitt, M.: A barrier to vertical mixing at 14 km in the tropics: Evidence from ozonesondes and aircraft measurements, J. Geophys. Res., 104, 22 095–22 102, 1999.

Geller, L. S., Elkins, J. W., Lobert, J. M., Clarke, A. D., Hurst, D. F., Butler, J. H., and Myers, R. C.: Tropospheric SF_6: Observed latitudinal distribution and trends, derived emissions and interhemispheric exchange time, Geoophys. Res. Lett., 24, 675–678, 1997.

Gloor, M., Dlugokencky, E., Brenninkmeijer, C., Horowitz, L., Hurst, D. F., Dutton, G., Crevoisier, C., Machida, T., and Tans, P.: Three-dimensional SF_6 data and tropospheric transport simulations: Signals, modeling accuracy, and implications for inverse modeling, J. Geophys. Res., 112, D15112, doi:10.1029/2006JD007973, 2007.

Hall, T. M. and Plumb, R. A.: Age as a diagnostic of stratospheric transport, J. Geophys. Res., 99, 1059–1070, 1994.

Hartley, D. E. and R. Black, Mechanistic analysis of interhemispheric transport, Geophys. Res. Lett., 22(21), 2945–2948, 1995.

Hasumi, H., Emori, S., Abe-Ouchi, A., et al., K-1 Coupled GCM (MIROC) Description, Technical report, CCSR, Kashiwa, Chiba, Japan, 2004.

Hoke, J. E. and Anthes, R. A.: The initialization of numerical models by a dynamic initialization technique, Mon. Weather Rev., 104, 1551–1556, 1976.

Holslag, A. A. M. and Boville, B.: Local versus nonlocal boundary-layer diffusion in a global climate model, J. Climate, 6, 1825–1842, 1993.

Jacob, D. J., Prather, M. J., Wofsy, S. C., and McElroy, M. B.: Atmospheric distribution of ^{85}Kr simulated with a general circulation model, J. Geophys. Res., 92, 6614–6626, 1987.

Kanamitsu, M., Ebisuzaki, W., Woolen, J., Potter, J., and Fiorino, M.: NCEP/DOE AMIP-II Reanalysis (R-2), B. Am. Meteorol. Soc., 83, 1631–1643, 2002.

Kida, H.: General circulation of air parcels and transport characteristics derived from a hemispheric GCM, Part 2, Very longterm motions of air parcels in the troposphere and stratosphere, J. Meteor. Soc. Japan, 61, 510–522, 1983.

Law, R. M., Peters, W., Rödenbeck, C., et al.: TransCom model simulations of hourly atmospheric CO_2: experimental overview and diurnal cycle results for 2002, Global Biogeochem. Cy., 22, GB3009, doi:10.1029/2007GB003050, 2008.

Levin, I. and Hesshaimer, V.: Refining of atmospheric transport model entries by the globally observed passive tracer distributions of 85krypton and sulfur hexafluoride (SF_6), J. Geophys. Res., 101, 16 745–16 756, 1996.

Lin, S.-J. and Rood, R.: Multidimensional flux-form semi-Lagrangian transport schemes, Mon. Weather Rev., 124, 2046–2070, 1996.

Lintner, B. R., Gilliland, A. B., and Fung, I. Y.: Mechanisms of convection- induced modulation of passive tracer interhemispheric transport interannual variability, J. Geophys. Res., 109, D13102, doi:10.1029/2003JD004306, 2004.

Maiss, M., Steele, L. P., Francey, R. J., Fraser, P. J., Langenfelds, R. L., Trivett, N. B. A., and Levin, I.: Sulfur hexafluoride – A powerful new atmospheric tracer, Atmos. Environ., 30, 1621–1629, 1996.

Mellor, G. L. and Yamada, T.: A hierarchy of turbulence closure models for planetary boundary layers, J. Atmos. Sci., 31, 1791–1806, 1974.

Miyazaki, K., Patra, P. K., Takigawa, M., Iwasaki, T., and Nakazawa, T.: Global-scale transport of carbon dioxide in the troposphere, J. Geophys. Res., 113, D15301, doi:10.1029/2007JD009557, 2008.

Nakazawa, T., Ishizawa, M., Higuchi, K., and Trivett, N. B. A.: Two curve fitting methods applied to CO_2 flask data, Environmetrics, 8, 197–218, 1997.

Numaguti, A., Takahashi, M., Nakajima, T., and Sumi, A.: Development of CCSR/NIES Atmospheric General Circulation Model, CGER's Supercomput, Monogr. Rep., 3, 1–48, Tsukuba, Ibaraki, 1997.

Olivier, J. G. J. and Berdowski, J. J. M.: Global emissions sources and sinks, in: The Climate System, edited by: Berdowski, J., Guicherit, R., and Heij, B. J., A. A. Balkema Publishers/Swets & Zeitlinger Publishers, Lisse, The Netherlands, ISBN 9058092550, 33–78, 2001.

Park, S., Jiménez, R., Daube, B. C., Pfister, L., Conway, T. J., Gottlieb, E. W., Chow, V. Y., Curran, D. J., Matross, D. M., Bright, A., Atlas, E. L., Bui, T. P., Gao, R.-S., Twohy, C. H., and Wofsy, S. C.: The CO_2 tracer clock for the Tropical Tropopause Layer, Atmos. Chem. Phys., 7, 3989–4000, 2007, http://www.atmos-chem-phys.net/7/3989/2007/.

Patra, P. K., Gurney, K. R., Denning, A. S., Maksyutov, S., Nakazawa, T., et al.: Sensitivity of inverse estimation of annual mean CO_2 sources and sinks to ocean – only sites versus all-sites observational networks, Geophys. Res. Lett., 33, L05814, doi:10.1029/2005GL25403, 2006.

Patra, P. K., Takigawa, M., and Ishijima, K.: An AGCM transport and multi-tracer based analysis of atmospheric CO_2, JPGU Annual Meeting, Chiba city, Japan, 2007.

Patra, P. K., Law, R. M., Peters, W., Rödenbeck, C., Takigawa, M., et al.: TransCom model simulations of hourly atmospheric CO_2: analysis of synoptic scale variations for the period 2002–2003, Global Biogeochem. Cy., 22, GB4013, doi:10.1029/2007GB003081, 2008.

Peters, W., Krol, M. C., Dlugokencky, E. J., Dentener, F. J., Bergamaschi, P., Dutton, G., Velthoven, P. v., Miller, J. B., Bruhwiler, L., Tans, P. P.: Toward regional-scale modeling using the two-way nested global model TM5: Characterization of transport using SF_6, J. Geophys. Res., 109, D19314, doi:10.1029/2004JD005020, 2004.

Postel, G. A. and Hitchman, M. H.: climatology of Rossby wave breaking along the subtropical tropopause, J. Atmos. Sci., 56, 359–373, 1999.

Prather, M., McElroy, M., Wofsy, S., Russell, G., and Rind, D.: Chemistry of the Global Troposphere: Fluorocarbons as Tracers of Air Motion, J. Geophys. Res., 92, 6579–6613, 1987.

Ravishankara, A. R., Solomon, S., Turnipseed, A. A., and Warren, R. F.: Atmospheric lifetimes of long-lived halogenated species, Science, 259, 194–199, 1993.

Rayner, N. A., Parker, D. E., Horton, E. B., Folland, C. K., Alexander, L. V., Rowell, D. P., Kent, E. C., and Kaplan, A.: Global analyses of sea surface temperature, sea ice, and night marine air temperature since the late nineteenth century, J. Geophys. Res., 108(D14), 4407, doi:10.1029/2002JD002670, 2003.

Rind, D., Lerner, J., Jonas, J., and McLinden, C.: Effects of resolution and model physics on tracer transports in the NASA Goddard Institute for Space Studies general circulation models, J. Geophys. Res., 112, D09315, doi:10.1029/2006JD007476, 2007.

Uhse, K., Meinhardt, F., and Ries, L.: Atmospheric SF_6 hourly concentration data, Schauinsland, in: World Data Centre for Greenhouse Gases, Japan Meteorological Agency, Tokyo, http://gaw.kishou.go.jp/wdcgg.html, 2006.

Uppala, S. M., Kållberg, P. W., Simmons, A. J., et al.: The ERA-40 re-analysis, Q. J. R. Meteor. Soc., 131, 2961–3012, doi:10.1256/qj.04.176, 2005.

WDCGG: WMO World Data Centre for Greenhouse Gases, Japan Meteorological Agency, Tokyo, data available at: http://gaw.kishou.go.jp, 2008.